1 Modelling of street-scale pollutant dispersion by coupled simulation of
2 chemical reaction, aerosol dynamics, and CFD

3   Chao Lin [a,*,★], Yunyi Wang [b,★], Ryozo Ooka [c], Cédric Flageul [d], Youngseob Kim [b],
4   Hideki Kikumoto [c], Zhizhao Wang [b], Karine Sartelet [b]
5 [a] Graduate School of Engineering, The University of Tokyo, 4-6-1 Komaba, Meguro-ku,
6 Tokyo 153-8505, Japan
7 [b] CEREA, École des Ponts ParisTech, EdF R&D, 77 455 Marne la Vallée, France
8 [c] Institute of Industrial Science, The University of Tokyo, 4-6-1 Komaba, Meguro-ku,
9 Tokyo 153-8505, Japan
10 [d] Curiosity Group, Pprime Institute, Université de Poitiers, CNRS, ISAE-ENSMA,
11 Chasseneuil, France
12 * Corresponding author, c-lin415@iis.u-tokyo.ac.jp
13 ★These authors contributed equally to this work.

15 ABSTRACT
16 In the urban environment, gas and particles impose adverse impacts on pedestrians' health.
17 The conventional computational fluid dynamics (CFD) methods that regard pollutant as
18 passive scalar cannot reproduce the formation of secondary pollutants and lead to
19 uncertain prediction. In this study, SSH-Aerosol, a modular box model that simulates the
20 evolution of gas, primary and secondary aerosols, is coupled with the CFD softwares
21 OpenFOAM and Code_Saturne. The transient dispersion of pollutants emitted from
22 traffic in a street canyon is simulated using unsteady Reynolds-averaged Navier–Stokes
23 equations (RANS) model. The simulated concentrations of NO_2, PM_{10} and black carbon
24 are compared with field measurements on a street of Greater Paris. The simulated NO_2
25 and PM_{10} concentrations based on the coupled model achieved better agreement with
26 measurement data than the conventional CFD simulation. Meanwhile, the black carbon
27 concentration is underestimated, probably partly because of the underestimation of non-
28 exhaust emissions (tyre and road wear). Aerosol dynamics lead to large increase of
29 ammonium nitrate and anthropogenic organic compounds from precursor-gas emitted in
30 the street canyon.

32 Keywords
33 Pollutant dispersion, Street canyon, Aerosol dynamics, CFD, PM_{10}, Secondary aerosols

1. Introduction
36 Traffic-related pollutants can impose adverse effects on pedestrians' health in the urban

37 environment (Anenberg et al., 2017; Jones et al., 2008). Especially, particulate matter
38 (PM) is strongly associated with increased cardiovascular diseases (Du et al., 2016).
39 Therefore, investigating the dispersion of PM and the corresponding precursor gas is of
40 great significance to evaluate the environmental impact and devise suitable
41 countermeasures (Kumar et al., 2008).
42 With the development of numerical simulations, computational fluid dynamics (CFD) has
43 been widely used for near-field dispersion prediction (Tominaga and Stathopoulos, 2013).
44 The pollutant dispersion patterns in complex geometric and non-uniform building
45 configurations can be well predicted using CFD simulations (Blocken et al., 2013).
46 Pollutant dispersion, deposition and transformation (chemical reactions and aerosol
47 dynamics) have primary roles in near-field prediction models. However, most CFD-based
48 studies assume that the time scale of transport at the street scale (~ 100 m) is relatively
49 shorter than the time scale of deposition and transformation; therefore, they frequently
50 regard pollutants as inert matter. Meanwhile, the recirculation flows which commonly
51 exist in street canyons lead to low-ventilation zones and may provide sufficient time for
52 transformation (Lo and Ngan, 2017; Zhang et al., 2020).
53 In addition, when PM is transported as a passive scalar, the distribution of the total
54 concentration can be simulated, however, information on the particle size distribution and
55 chemical composition is unclear. Understanding the size distribution is important for
56 evaluating the health hazards because large particles are deposited in the mouth and upper
57 airways, whereas smaller particles deposit deeper in the lungs and can even reach the
58 alveolar region of the lungs (Sung et al., 2007). In addition, as particles of different
59 chemical compositions are related to different sources and/or precursor gases, gaining
60 knowledge of their composition may help devise countermeasures to limit their
61 concentrations (Kim, 2019).
62 To simulate pollutant concentrations considering both transport and transformation, many
63 studies have coupled air-quality models with gas-phase chemistry and aerosol modules
64 and achieved chemical transport from a regional scale (~100 km) (Sartelet et al., 2007) to
65 a street scale (Lugon et al., 2021b). However, few models can simultaneously represent
66 detailed particle dispersion in a complicated urban flow field considering secondary
67 aerosol formation.
68 For the recent development and application of CFD-chemistry coupling model, Kurppa
69 et al., (2019) implemented a sectional aerosol module into large eddy simulation (LES),
70 and conducted a particle dispersion simulation on a neighborhood scale. Gao et al., (2022)
71 employed the same model to examine the dispersion of cooking-generated aerosols in an
72 urban street canyon. In both studies, the effect of particle dynamics on aerosol number

concentration was well reproduced. However, the simulated chemical composition was not detailed. In addition, the chemical reactions of the precursor gas were not considered. Kim et al., (2019) coupled unsteady Reynolds-averaged Navier-Stokes (RANS) model with gas chemistry and aerosol modules and conducted simulations of PM_1 in a street canyon under summer and winter conditions. The diurnal variations, spatial distribution and chemical composition of pollutants in the street canyon were investigated. However, the size distribution of particles and the secondary organic aerosol (SOA) chemistry were not considered. Therefore, a more comprehensive coupled model is needed to simulate the evolution of gas concentrations, mass and number concentrations of primary and secondary particles at the same time.

Vehicles are considered to be the main ammonia (NH_3) source in urban environments (Sun et al., 2017). Reactive nitrogen emissions from many new vehicles are now dominated by NH_3 (Bishop and Stedman, 2015). Since the formation of ammonium nitrate is often limited by HNO_3 rather than NH_3 in urban areas (NH_3-limited), increasing NH_3 may lead to increased ammonium nitrate production and PM concentration in urban streets (Lugon et al., 2021b). However, NH_3 emissions from passenger cars are usually not regulated (Suarez-Bertoa and Astorga, 2018). Therefore, to provide evidence in making policies for NH_3 emission regulation, it is important to investigate the local influence of NH_3 emissions on PM concentrations.

Therefore, to achieve a more comprehensive simulation of PM and related precursor gas, this study couple two open-source CFD softwares: OpenFOAM (OpenFOAM user guide) and Code_Saturne (Archambeau et al., 2004), with gas-phase chemistry and aerosol module SSH-Aerosol (Sartelet et al., 2020). Both OpenFOAM and Code_Saturne own wide users. Therefore, coupling SSH-aerosol with both CFD softwares may satisfy more needs. Simulations of the PM concentrations in a two-dimensional street canyon are conducted. The coupled model is validated by comparison to field measurements. The size distributions and chemical compositions of particles from the models with and without secondary aerosol formation are compared. In addition, cases with large NH_3 emissions are considered and the related PM increase is investigated.

The remainder of this paper is organized as follows. The coupling of the aerosol model and CFD is introduced in Section 2. The computational details are presented in Section 3. In Section 4, the simulated pollutant concentrations are compared with field measurements, followed by evaluations of the influence of the grid, coupling method and time step. In Section 5, spatial and temporal variations in the concentrations are analyzed. The chemical compositions and size distributions of the particles between the coupled model and the model that does not consider gas chemistry or aerosol dynamics are

109 compared. In addition, the effect of NH_3 traffic emissions on particle concentrations is
110 discussed. Finally, the conclusions and perspectives are presented in Section 6.
111
112 **2. Model description**
113 The coupling method between CFD and chemistry modules is similar to the literature
114 (Gao et al., 2022; Kurppa et al., 2019). OpenFOAM v2012 and Code_Saturne 6.2 are
115 used to solve the governing equations of the flow field and transport equations of gas and
116 particle mass fractions. The inflow conditions, pollutants' background concentrations and
117 emission rates are obtained from regional models, and are linearly interpolated into each
118 time step, which will be introduced in Section 3. This simulation method is called
119 transient-condition method (TCM) in this study. However, because time-varying flow
120 fields and concentration fields are expensive to compute in terms of computational time,
121 conducting CFD simulations with fixed boundary conditions and emission rates at
122 specific time points is considered a practical method for evaluating street-level pollutant
123 concentrations (Wu et al., 2021; Zhang et al., 2020). The transport (advection and
124 diffusion) and chemical processes will reach equilibrium, and the simulated
125 concentrations will reach quasi-stable values. These values are often regarded as time-
126 averaged concentrations. This method is called the constant-condition method (CCM) in
127 this study, in contrast to TCM. However, the simulation accuracy of CCM has not been
128 validated in simulations that consider both gas chemistry and particle dynamics.
129 Therefore, validation is conducted using boundary conditions and emission rates at
130 specific time points and the simulated concentrations with CCM and TCM are compared
131 in Section 4.2.
132 The unsteady RANS model is used for the transient simulations with both CFD codes. In
133 OpenFOAM, the RNG (Re-Normalisation Group) k–ε model (Yakhot et al., 1992) is
134 deployed for turbulence closure. All transport equations are discretized using the total
135 variation diminishing (TVD) scheme (Harten, 1984; Yee, 1987), which combines the
136 first-order upwind difference scheme and the second-order central difference scheme. The
137 PIMPLE algorithm, a merged PISO (Pressure Implicit with Splitting of Operator)–
138 SIMPLE (Semi-Implicit Method for Pressure-Linked Equations) algorithm in the
139 OpenFOAM toolkit, is used for pressure–velocity coupling. In Code_Saturne, turbulence
140 is solved using the k–ε turbulence model (linear production) (Guimet and Laurence, 2002).
141 The time and space discretizations of velocity, pressure and other scalars in all transport
142 equations are realized through a centred scheme and a fractional step scheme
143 (Archambeau et al., 2004) . For both CFD software, the dry deposition schemes for gas
144 and particle are added to the transport equations using volume sink terms based on Zhang

145   et al. (2003) and Zhang et al. (2001), respectively. The details of the implementation are

146   provided in Appendix A.

147   SSH-Aerosol (Sartelet et al., 2020) is a modular box model that simulates the evolution

148   of not only gas concentrations but also the mass and number concentrations of primary

149   and secondary particles. In SSH-Aerosol 112 gas species and 40 particle species are

150   considered. The particle compounds are dust, black carbon, inorganics (sodium, sulphate,

151   ammonium, nitrate and chloride), primary organic aerosol (POA) and secondary organic

152   aerosol (SOA). Three main processes involved in aerosol dynamics (coagulation,

153   condensation /evaporation and nucleation) are included. The particle size distribution is

154   modelled using a sectional size distribution. Nucleation is not considered in this study

155   because only the mass and not the number of particles is available for evaluation, and

156   large uncertainties remain on the nucleation parameterizations (Sartelet et al., 2022)

157   mostly affecting the number of particles. As nucleation is not considered, the minimum

158   diameter does not need to be as low as 0.001 μm, and it is fixed to 0.01 μm, as in the

159   regional-scale simulations of Sartelet et al. (2018), which provide the background

160   concentrations. Six particle size sections are employed with bound diameters of 0.01, 0.04,

161   0.16, 0.4, 1.0, 2.5 and 10 μm.

162   The coupling between CFD and SSH-aerosol are achieved by using the application

163   program interface (API) of SSH-aerosol. The gas and particle concentrations are

164   initialized in CFD and are transported in the domain for each time step. For each grid

165   volume cell, these transported concentrations, as well as meteorological parameters, such

166   as temperature and humidity, are then sent to SSH-aerosol to advance one time step of

167   gaseous chemistry and aerosol dynamics. Once the SSH-aerosol calculation is completed,

168   the concentrations are sent back to the CFD for the next time step. It should be noted that

169   as the SSH-aerosol processes the ensemble-averaged concentration from RANS model,

170   the covariance of turbulent diffusion and chemical reaction may not be fully reproduced.

171   The influence of different operator splitting algorithms is discussed in Section 4.4.

172

173 **3. Simulation setup**

174
175 Fig. 1 Simulation domain of street canyon

176

177 The simulation is set up to model a street in Greater Paris (Boulevard Alsace-Lorraine),
178 where field measurements were conducted from April 6 to June 15, 2014. The
179 concentrations of nitrogen dioxide (NO_2), particles with diameters less than 10 μm (PM_{10}),
180 and black carbon were measured as described in (Kim et al., 2018). Fig. 1 shows the
181 simulation domain. The 2-D street canyon is 27.5 m in width (W) and 8.5 m in height
182 (H). The domain height is 6 H. The street canyon is discretized into uniform grids in x-
183 and z- directions. The grid resolutions in the street canyon are 0.5 m in both x-and z-
184 directions, respectively. The largest grid sizes are 4 m (x) × 2m (z). An analysis of the
185 grid sensitivity is described in Section 4.3.
186 Simulations are conducted from 4:30 a.m. to 5 p.m. on April 30, 2014 at local time
187 (GMT+2). This period is selected because the wind direction is almost perpendicular to
188 the street canyon during that day, allowing for a 2D simulation setting. During the field
189 measurement, there exists several time periods that the wind direction is perpendicular
190 with the street canyon. Meanwhile, some time periods are short (less than 5 hours), and
191 we consider that short period simulation is not representative in simulation accuracy. In
192 addition, we consider that it is critical to have a simulation time long enough to cover
193 both day-time chemistry and night-time chemistry. The first 30 minutes of the simulation
194 corresponds to model spin-up, and the simulation lasts 12 hours. A sensitivity analysis of
195 numerical aspects, such as the splitting method between transport and chemistry and the
196 time step, is described in Section 4.4.

Fig. 2 Time variations of hourly friction velocity and temperature for inflow.

Meteorological conditions (Fig. 2) including time-varying friction velocity and temperature are obtained from the simulation described in Sartelet et al. (2018) using the Weather Research and Forecasting (WRF) model. The grid resolution is 1 km ×1 km in Paris. The lowest and highest friction velocities occurred approximately at 5 a.m. and 11 a.m., respectively. The lowest and highest temperatures are around 8 a.m. and 5 p.m. For the inflow, the wind direction is perpendicular to the street canyon. The friction velocity u_* is used to prescribe the vertical profiles of the streamwise velocity U, turbulent kinetic energy k and turbulent dissipation rate ε as follows

$$U(z) = \frac{u_*}{\kappa} \ln\left(\frac{z - H}{z_0}\right) \tag{1}$$

$$k(z) = \frac{u_*^2}{\sqrt{C_\mu}} \tag{2}$$

$$\varepsilon(z) = \frac{u_*^3}{\kappa(z - H)} \tag{3}$$

where κ is the von Kármán constant and C_μ is the model constant (=0.09) in the k-ε model. The roughness length z_0 is set to 1 m for the inlet (Belcher, 2005) and 0.1 m for the wall and bottom (Lo and Ngan, 2015).

In addition, since the domain height is low (51 m) in this study and we focus on the pollutant dispersion behaviors in the street canyon, it is reasonable to consider the atmospheric stability as neutral; therefore the temperature is assumed to be spatially uniform at the inflow. The hourly friction velocities and temperatures are linearly interpolated into each timestep and prescribed at the inflow.

217
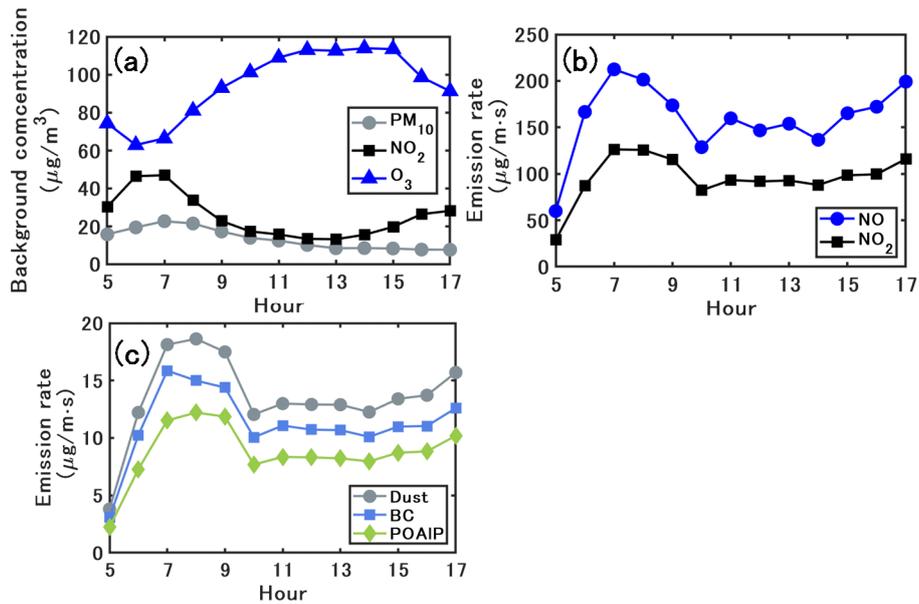
Fig. 3 Time variations of (a) PM_{10}, NO and NO_2 background concentrations, (b) emission
rates of NO and NO_2 and (c) emission rates of dust, BC and organics (POAlP).

220

Fig. 3(a) shows the time variations of the PM_{10}, NO and NO_2 background concentrations.
Fig. 3(b) and (c) show the emission rates for NO, NO_2 and the emitted compounds of
PM_{10}. The background concentrations of the gas and particles are obtained from the
regional-scale simulations of Sartelet et al. (2018) with the Eulerian model Polair3D of
the Polyphemus air quality modelling platform (Mallet et al., 2007), which uses the same
chemical representation as in this study. As detailed in Sartelet et al. (2018), the regional
background concentrations compare well to measurements of O_3, NO_2, PM_{10}, $PM_{2.5}$,
black carbon and organic aerosols. The hourly background concentrations are linearly
interpolated into each timestep and prescribed at the inflow and top. The traffic emission
source is assumed to be approximately 14 m in width and 1.5 m in height, and it is set in
the middle of the bottom of the canyon (Fig. 1). As detailed in Kim et al. (2022), emissions
are estimated from the fleet composition and the number of vehicles in the street using
COPERT's emission factors (COmputer Program to calculate Emissions from Road
Transport, version 2019, EMEP/EEA, 2019). After the speciation of NO_x, Volatile
Organic Compounds (VOC), $PM_{2.5}$ and PM_{10} into model species, emissions are set for 16
gaseous model species and three particle model species: dust and unspecified matter
(Dust), black carbon (BC) and primary organic aerosol of low volatility (POAlP). The
PM size distribution at emission is assumed to be the same as in the previous studies
(Lugon et al., 2021a, 2021b). The exhaust primary PM is assumed to be in the size bin
[0.04 – 0.16 µm] while non-exhaust primary PM is coarser in the size bin [0.4 – 10 µm].

250 The turbulent Schmidt number Sc_t in the concentration transport equations, which is the
251 ratio of the turbulent diffusivity to the concentration and turbulent kinematic viscosity, is
252 important in turbulent diffusion modeling. The value of Sc_t is considered between 0.2
253 and 1.3, depending on the flow properties and geometries (Tominaga and Stathopoulos,
254 2007). For urban environments with a compact layout, a small $Sc_t = 0.4$ is found to
255 show better agreement with wind tunnel experiment data (Di Sabatino et al., 2007).
256 Therefore, a value of 0.4 is adopted in the current study.

257

4. Model evaluation

4.1. Validation with field measurements and comparison of simulated concentrations with the two CFD software

267

269 wind velocity is not available. Therefore, we conducted a velocity validation for
270 OpenFOAM v2012 using data from a wind tunnel experiment (Blackman et al., 2015).
271 The predicted mean velocity agreed well with the experimental values. The details can be
272 found at Appendix B.
273 Fig. 4 compares the simulated concentrations with those obtained from the field
274 measurements. In the field measurements, the measured concentration was obtained from
275 averaging over two measurement points near the leeward and windward walls in the street
276 canyon. In this section, the simulated results and discussion are based on the spatially-
277 averaged values in the street canyon ($27.5 \leq x \leq 55, 0 \leq z \leq 8.5$ m). CFD-passive and
278 CFD-chemistry denote the CFD simulation without and with chemistry coupling. OF and
279 CS denote simulated concentrations based on OpenFOAM and Code_Saturne. The
280 operator splitting order and time step for OF and CS are the A-B-A splitting method with
281 0.5 s and the A-B splitting method with 0.25 s, as detailed in Section 4.4. The simulation
282 time ratio of CFD-chemistry and CFD-passive is about three times in both OpenFOAM
283 and Code_Saturne in this study.
284 For NO_2, the peak concentration in the field measurement occurred approximately at 7
285 a.m. owing to the morning traffic. In the CFD-passive simulations, the lack of chemical
286 reactions lead to an underestimation of NO_2, while the concentrations simulated with
287 CFD-chemistry agree well with the measurements. For PM_{10}, the concentrations
288 simulated with CFD-chemistry also show better agreement with the measurements than
289 CFD-passive. The primary reason is that CFD-chemistry can reproduce the condensation
290 of inorganic and organic matter from the gas phase to the particle phase, which will be
291 further explained in the following sections. The simulation results based on OF and CS
292 show small differences, and detailed comparisons are presented in Fig. 6.
293 Validation metrics (Chang and Hanna, 2004) are used to quantify the overall accuracy of
294 the CFD simulated concentrations based on OF, compared with the measured values
295 (Trini Castelli et al., 2018; Ferrero et al., 2019). The following metrics are used: fractional
296 bias (FB), geometric mean bias (MG) and normalized mean square error (NMSE). These
297 metrics are defined as follows:

$$\text{FB} = \frac{\overline{Obs} - \overline{CFD}}{0.5(\overline{Obs} + \overline{CFD})} \qquad (4)$$

$$\text{MG} = \exp(\overline{\ln Obs} - \overline{\ln CFD}) \qquad (5)$$

$$\text{NMSE} = \frac{\overline{(Obs_i - CFD_i)^2}}{\overline{Obs} \times \overline{CFD}} \qquad (6)$$

298 where Obs_i and CFD_i are the measured and CFD simulated concentrations for the
299 compound/species i, respectively. The overbar represents the mean value of the entire

300   dataset. The ideal values are 1 for MG, and 0 for FB and NMSE. Previous research has

301   suggested that $|FB| < 0.3,\ 0.7 < MG < 1.3$ and NMSE < 4 are acceptable for

302   simulated concentrations (Hanna et al., 2004).

303   Table 1 shows the statistical indicators for spatially averaged concentrations of NO_2 and

304   PM_{10} in the street canyon from 5 a.m. to 5 p.m. For NO_2 and PM_{10}, the mean and 90%

305   percentile concentrations simulated with CFD-chemistry are closer to the measurements

306   than those simulated with CFD-passive. In addition, the FB, MG and NMSE values of

307   CFD-chemistry are closer to the ideal values than those of CFD-passive.

308

309   Table 1 Statistical indicators for NO_2 and PM_{10} in the street canyon from 5 a.m. to 5p.m.

310   The concentrations are simulated with OpenFOAM.

	Concentration (µg/m³)		Validation metrics		
NO₂	Mean	Percentile 90%	FB	MG	NMSE
Measurement	66.6	91.8	/	/	/
CFD-chemistry	67.3	97.3	-0.01	1.00	1E-4
CFD-passive	45.9	73.7	0.36	1.50	0.14
PM₁₀	Mean	Percentile 90%	FB	MG	NMSE
Measurement	26.4	32.5	/	/	/
CFD-chemistry	22.3	33.1	0.17	1.23	0.03
CFD-passive	18.8	28.9	0.34	1.45	0.13

311
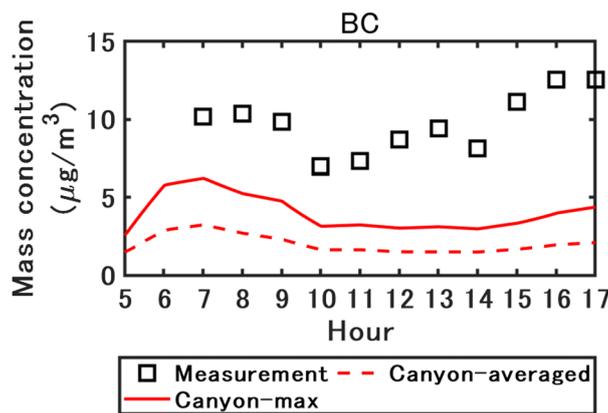
313   Fig. 5 Measured and simulated black carbon concentrations with OpenFOAM. The

314   canyon-averaged and maximum concentrations in the street canyon are represented by

315   the plain line and the dashed line respectively ($27.5 \leq x \leq 55, 0 \leq z \leq 8.5$ m).

316

317   The black carbon (BC) concentration simulated with OF is compared with the

318   measurements in Fig. 5. Because BC is considered an inert matter, considering chemistry
319   does not influence the mass concentration. Therefore, the concentrations simulated with
320   CFD-passive and CFD-chemistry show little difference; only the concentration simulated
321   with CFD-chemistry is shown here. The BC concentrations are underestimated by a factor
322   of approximately 5. Even the maximum concentrations in the street canyon largely
323   underestimate the measurements. One of the causes of this underestimation may be the
324   underestimation of the non-exhaust tyre emission factors in the COPERT emission factors
325   used here (Lugon et al., 2021a).
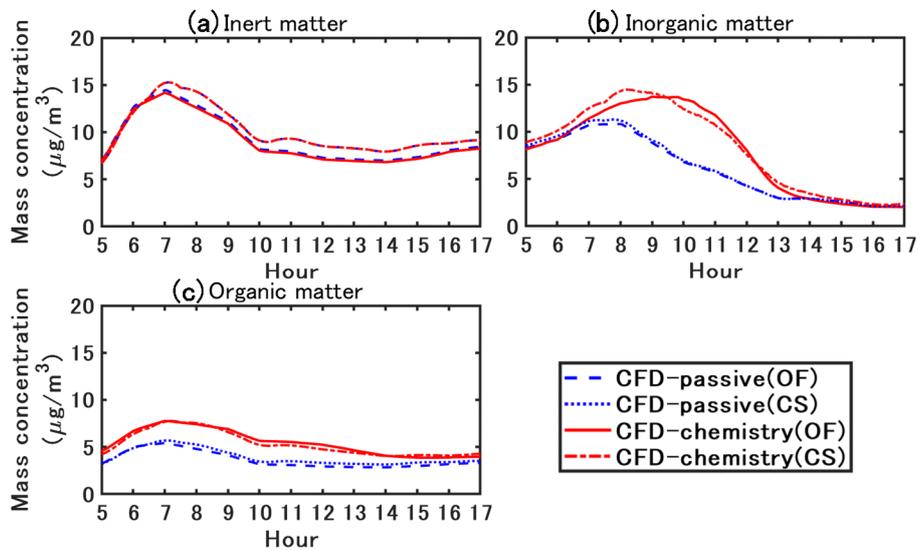
326
327   Fig. 6 Simulated particle concentrations with OpenFOAM (OF) and Code_Saturne (CS).
328   CFD-passive and CFD-chemistry denote the CFD simulation without and with chemistry
329   coupling.
330
331   The particle concentrations simulated with OF and CS are compared in Fig. 6. The
332   evolutions of the concentrations simulated by OF and CS are similar. Higher PM_{10}
333   concentrations are simulated by CS around 8 a.m. during the traffic peak and in the
334   afternoon, mostly because of the higher concentrations of emitted inert compounds, such
335   as black carbon and dust. Differences in the turbulence scheme may explain these
336   variations. Meanwhile, the difference between CFD-passive and CFD-chemistry for the
337   inorganic and organic matter is in accordance with OF and CS, showing the robustness
338   of the coupling method between CFD and SSH-aerosol by API. For simplicity, only the
339   simulated concentration based on OF is presented and discussed in the following sections.
340

341   *4.2. Transient-condition method and constant-condition method*
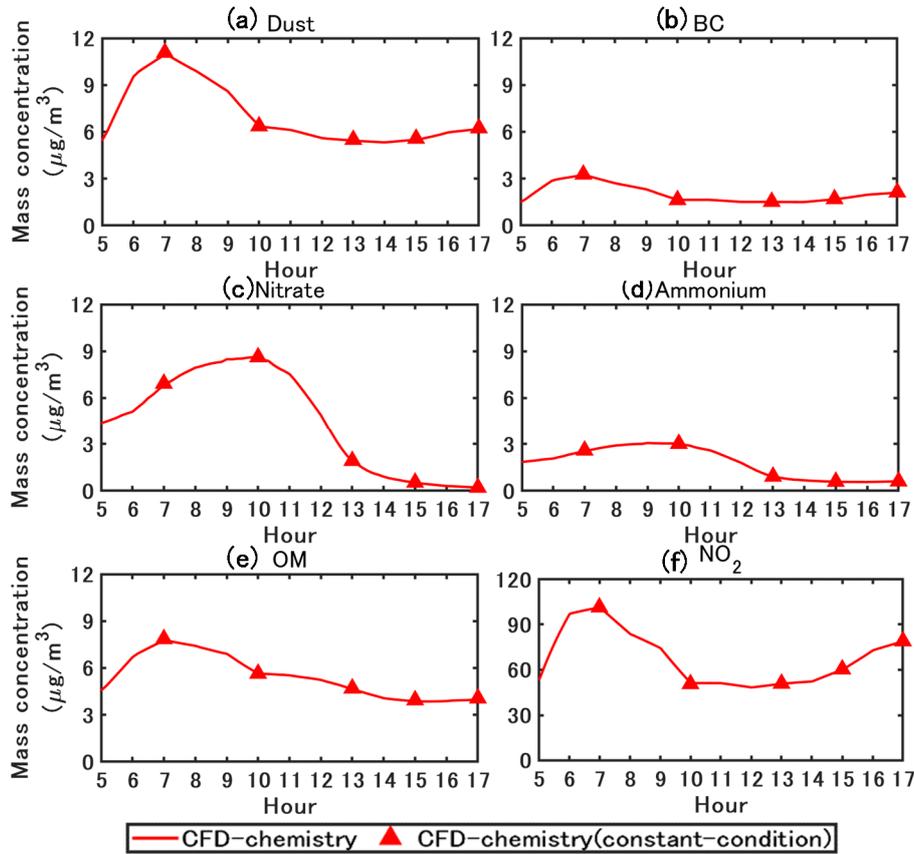
342

343   Fig. 7 Simulated PM$_{10}$ and NO$_2$ concentrations with the transient-condition and constant-
344   condition methods. The concentrations are spatially averaged in the street canyon.

345

346   To validate the simulation accuracy of CCM in simulations that consider both gas
347   chemistry and particle dynamics, simulations are conducted using boundary conditions
348   and emission rates at five time points (7 a.m., 10 a.m., 1 p.m., 3 p.m. and 5 p.m.). Other
349   simulation conditions, including the grid, coupling method, and time step, are the same
350   as the transient-condition simulation.
351   In Fig. 7, for PM$_{10}$ and NO$_2$, the concentrations simulated with CCM (red triangles) are
352   similar to those simulated with TCM. In addition, depending on the background
353   concentration and emission conditions, the simulation time required for CCM to reach
354   dynamic equilibrium is less than 1000 time steps (approximately 500 s). Therefore, CCM
355   can be utilized for parameter studies. The sensitivity analysis of the grid, coupling method
356   and time step in Section 4.3 and 4.4 is based on CCM. However, CCM should be used
357   with caution when the inflow wind speed and direction vary rapidly. The simulated
358   concentrations in Section 5 are based on TCM.

359

360   *4.3. Grid sensitivity*
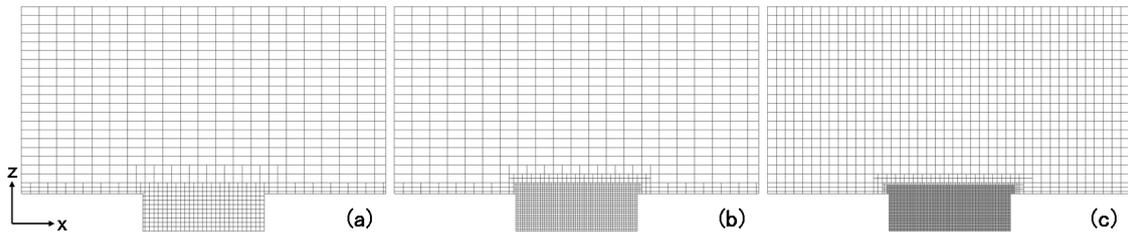
361

362   Fig. 8 Different grid resolutions for sensitivity analysis: (a) coarse, (b) basic, (c) fine. The
363   grid resolutions in the street canyon are 1 m, 0.5 m and 0.25 m in both x-and z- directions,
364   respectively. The largest grid sizes are 4 m (x) × 2m (z) in the coarse and basic grids,
365   and 2 m (x) × 2m (z) in the fine grid.

366

367   Grid sensitivity analysis is conducted based on three different resolutions as shown in Fig.
368   8. The grid resolutions in the street canyon for coarse, basic and fine grids are 1 m, 0.5 m
369   and 0.25 m in both x-and z- directions, respectively. The largest grid sizes are 4 m (x) ×
370   2m (z) for the coarse and basic grids, and 2 m (x) × 2m (z) for the fine grid. The
371   simulations are based on constant-condition method. The A-B-A splitting method, which
372   is introduced in Section 4.4, is used with a time step of 0.5 s. Fig. 9 shows the comparative
373   results for the mass concentration. No significant discrepancy is observed between the
374   different grids for NO_2, inert matter and organic matter. Meanwhile, the simulated
375   inorganic matter based on coarse grids shows slightly smaller concentrations than the
376   other grid resolutions, while the concentrations based on basic and fine grids are close.
377   Therefore, the basic grid is adopted for simulations in this study.
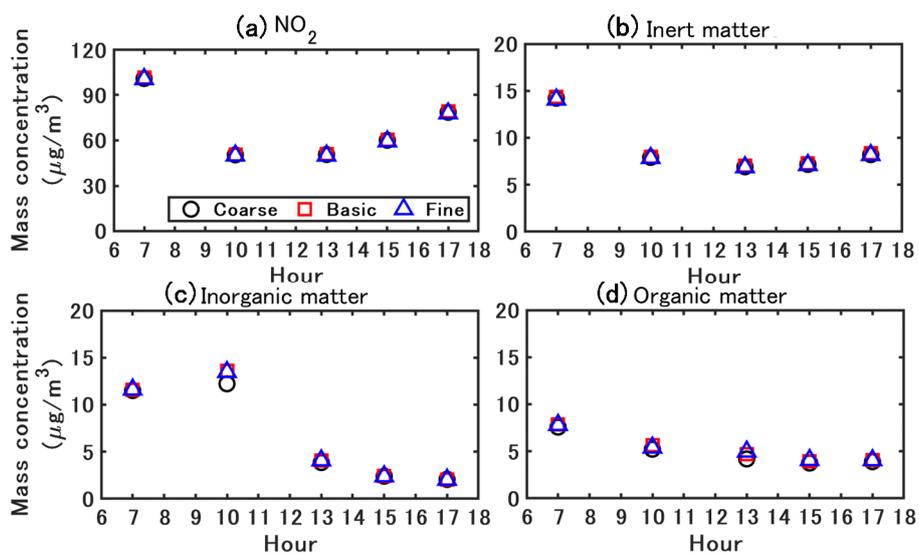
378
379   Fig. 9 Simulated NO_2 and particle concentrations with different grid resolutions.

380

381 *4.4. Coupling method and time step sensitivity*

382 The transport equation for the chemical species includes terms of advection, diffusion,
383 emission and chemical reactions. Ideally, the transport equation should be solved with all
384 the above terms, that is, by coupling all processes. However, the chemical process is
385 integrated with a stiff integrator, whereas advection, diffusion and emission are integrated
386 with a flux scheme. Therefore, operator splitting (Sportisse, 2000) is often employed to
387 solve different terms individually and sequentially over a given time step in chemical
388 transport simulations (Fu and Liang, 2016).

389 In this study, advection, diffusion and emission are simultaneously solved in CFD, and
390 the chemical reactions including gas chemistry, particle dynamics and size redistribution
391 are solved in SSH-Aerosol. Two operator-splitting orders are considered for coupling: A-
392 B splitting and A-B-A splitting (Sportisse, 2000). For A-B splitting, which can be
393 summarized as CFD(Δt)-Chemistry(Δt), the mass concentrations are first integrated for
394 transport over a time step Δt. The updated concentrations are then integrated for
395 chemistry at the same Δt. On the other side, A-B-A splitting adopts a symmetric sequence
396 of operators, which can be summarized as CFD($\Delta t/2$)-Chemistry(Δt)-CFD($\Delta t/2$). The
397 mass concentrations are first integrated for transport over a half time step, then for
398 chemistry over the full time step and finally for transport again over a half time step.

399

400 Table 2 Relative change in the computation time with different operator-splitting order
401 and time steps. The computation time is normalized by ABA-05.

Case	Operator splitting order	Δt (s)	Change in the computation time
AB-05	A-B splitting CFD(Δt)-Chemistry(Δt)	0.5	0.90
AB-025		0.25	1.56
ABA-1	A-B-A splitting CFD($\Delta t/2$)-Chemistry(Δt)-CFD($\Delta t/2$)	1	0.57
ABA-05		0.5	1
ABA-025		0.25	2.44

402

403 A sensitivity analysis is conducted on the operator splitting method and splitting time step.
404 As shown in Table 2, the time step is considered 0.5 s and 0.25 s for the A-B splitting
405 (named AB-05 and AB-025), and 1 s, 0.5 s and 0.25 s for the A-B-A splitting (named
406 ABA-1, ABA-05 and ABA-025). The simulated NO_2 and particle concentrations are
407 presented in Fig. 10. ABA-1 and AB-05 concentrations hardly differ from the figures.
408 Meanwhile, the computational time of ABA-1 is only 63% of that of AB-05. Similarly,
409 the concentrations simulated with ABA-05 and AB-025 are almost the same, and the

 computational time of ABA-05 is only 64% of AB-025. Therefore, the A-B-A splitting
411 method can be considered as a cost effective method.

412
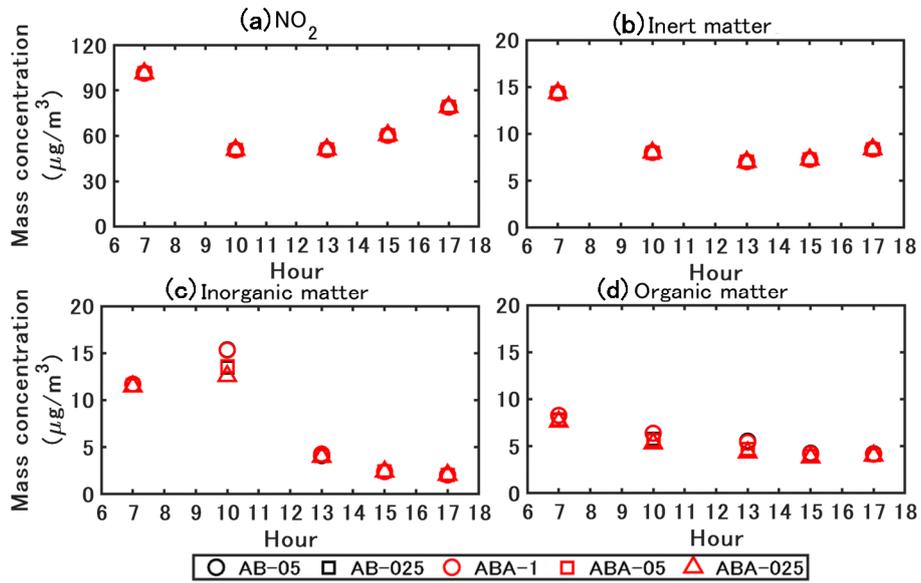
413

414 Fig. 10 Simulated NO_2 and particle concentrations with different coupling methods and
415 time steps. ABA denotes the A-B-A splitting method: CFD(Δt/2)-Chemistry(Δt)-
416 CFD(Δt/2). AB denotes the A-B splitting method: CFD(Δt)-Chemistry(Δt). In the legend,
417 the values that follow the capital letter ABA or AB denote the time step Δt (in s) used in
418 the simulation.

419

420 The concentrations simulated with the A-B-A splitting method and different time steps
421 show that small time step results in low inorganic and organic matter concentrations. The
422 concentrations simulated with ABA-1 are larger than those of ABA-05, and larger than
423 ABA-025. However, the differences between the concentrations simulated with ABA-05
424 and ABA-025 are lower than the differences between ABA-1 and ABA-05. For NO_2 and
425 inert particles, no obvious difference is found between the simulations with different
426 splitting methods and splitting time steps. Therefore, the A-B-A splitting method with a
427 time step of 0.5 s is adopted in this study.

428

5. Results and discussion

5.1. Time-averaged flow field and concentration field
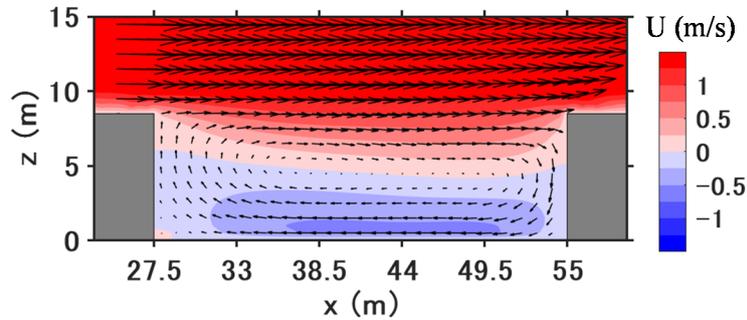
Fig. 11 Time-averaged flow field in the street canyon from 5 a.m. to 5 p.m.

This section shows the results for time-averaged values from 5 a.m. to 5 p.m. Fig. 11 shows the 12-hour time-averaged streamwise velocity and wind direction in the street canyon. At the current aspect ratio (H/W=0.31), a large vortex is observed in the canyon with a small secondary vortex at the corner of the leeward wall. A reverse flow is observed in the lower half of the canyon.
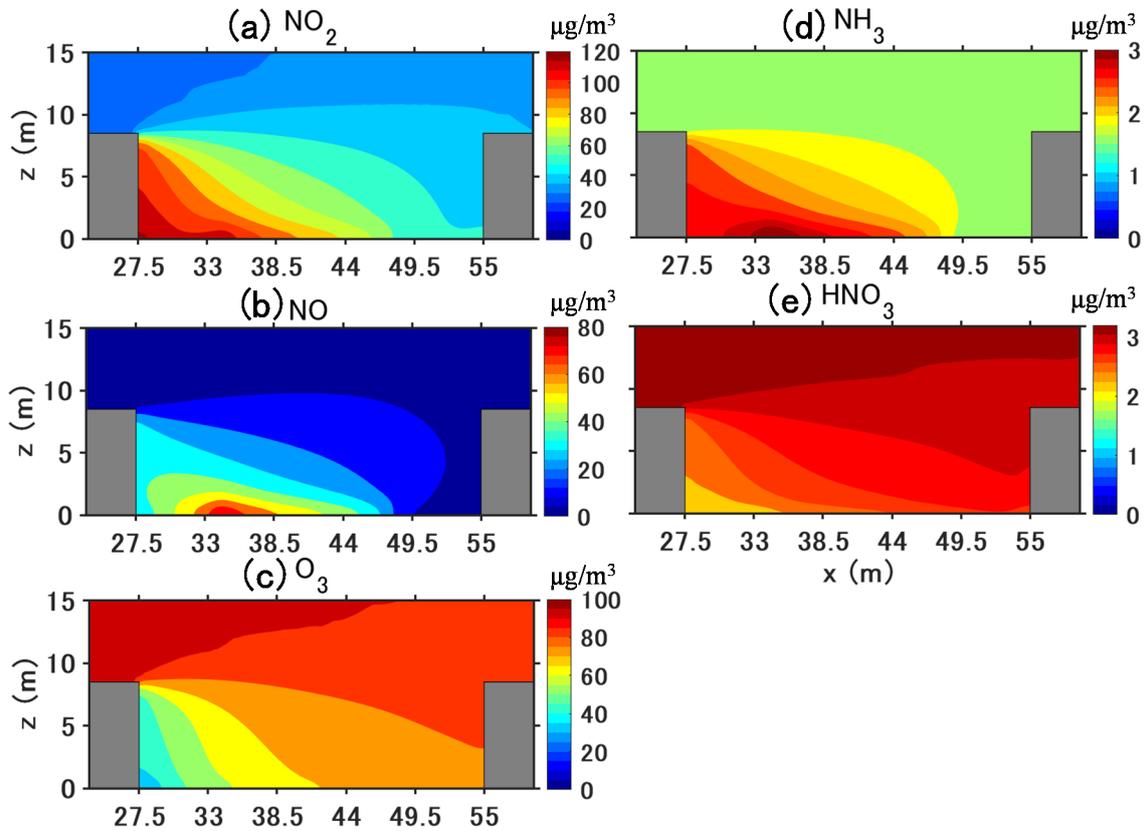
Fig. 12 Time-averaged concentrations ($\mu g/m^3$) of gaseous pollutants in the street canyon

441 from 5 a.m. to 5 p.m.

442

443 Fig. 12 shows the time-averaged concentrations of the gaseous pollutants from 5 a.m. to
444 5 p.m. For gaseous pollutants emitted by traffic, such as NO_2, NO and NH_3, larger
445 concentrations are found in the street, particularly near the leeward wall, compared to the
446 windward wall due to the reverse flow. Simultaneously, gas-phase chemistry and
447 condensation/evaporation between the gas and particle phases also influence the
448 concentration distribution. NO_2 mainly increases due to chemical production from NO
449 emissions and background O_3. Compared to the background NO_2 concentration of 26
450 $\mu g/m^3$, the longest retention time at the leeward side corner leads to the street canyon's
451 largest concentration (121 $\mu g/m^3$). At pedestrian height (z=1.5 m), NO_2 concentration is
452 116 $\mu g/m^3$ at the leeward wall and 49 $\mu g/m^3$ at the windward wall.
453 However, NO and NH_3 generally decrease because of loss by gaseous chemistry and the
454 condensation of ammonium nitrate, respectively; therefore, the largest concentrations are
455 at the leeward corner of the traffic emission source. For secondary gaseous pollutants
456 without traffic emissions such as O_3 and HNO_3, gaseous chemistry and condensation lead
457 to lower concentrations in the street canyon than background concentrations. For O_3, this
458 is due to the titration of O_3 by NO, whose concentration is large near the leeward wall.
459 For HNO_3, this is because of the high concentrations of NH_3, which then condenses with
460 HNO_3 to form ammonium nitrate. In addition, the lowest concentration of O_3 and HNO_3
461 can be found at the leeward corner which corresponds to the secondary vortex in Fig. 11,
462 indicating that the pollutant residence time is the highest in that corner leading to enhance
463 ozone titration.
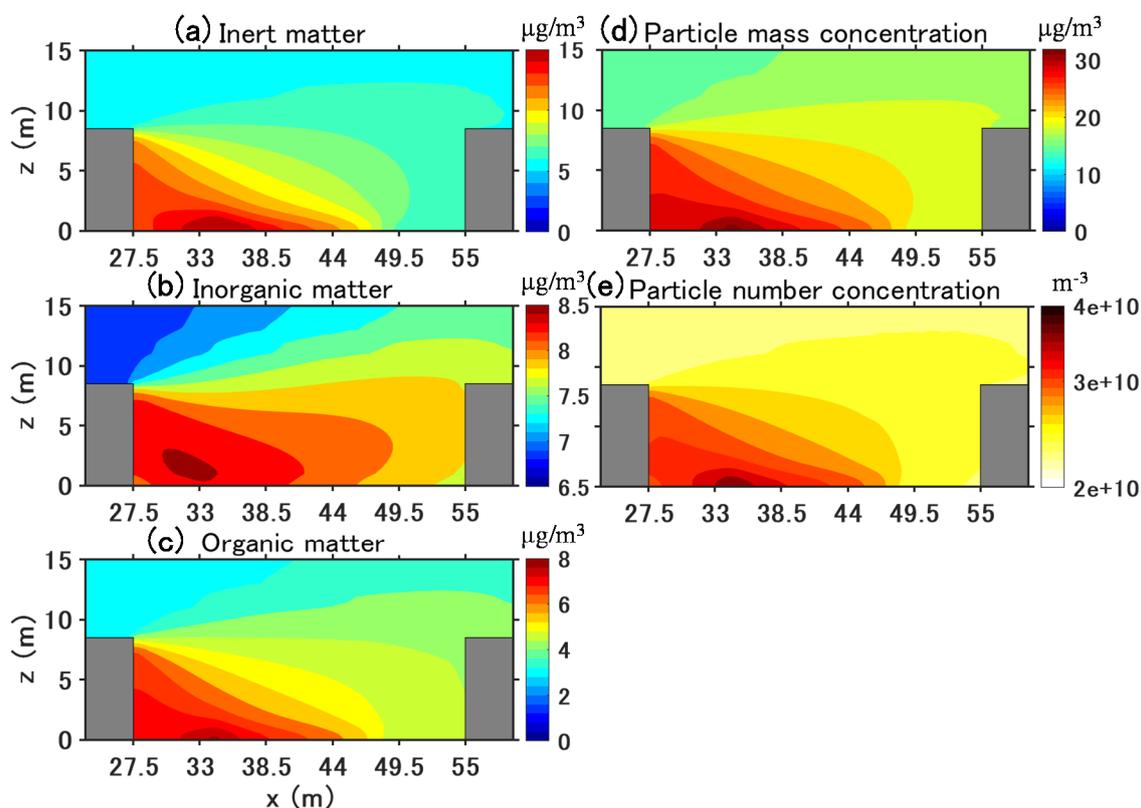
464
465 Fig. 13 Time-averaged concentrations of particle number, mass and composition in the
466 street canyon from 5 a.m. to 5 p.m. The unit is μg/m³ for mass concentration and m⁻³ for
467 number concentration.
468
469 Fig. 13 shows the time-averaged PM$_{10}$ mass concentration, and the number
470 concentrations and PM composition (inorganic, organic and inert matter) from 5 a.m. to
471 5 p.m. For inert and organic matter, the highest concentrations are near the leeward corner
472 of the traffic emission source. Because inorganic matter is not emitted, the concentration
473 distribution differs from inert and organic matter. However, as they are produced from
474 gas condensation and strongly influenced by traffic emissions, the highest concentrations
475 are observed in the leeward corner.
476 At pedestrian height (z=1.5 m), the PM$_{10}$ mass concentration is approximately 28 μg/m³
477 at the leeward wall and 19 μg/m³ at the windward wall, which is larger than the
478 background concentration of 15 μg/m³. The number concentration is computed from the
479 mass concentration and therefore has a similar spatial distribution as PM$_{10}$ mass
480 concentration (nucleation from gas was not taken into account). Traffic emission
481 significantly increases the number concentration. The number concentration is about
482 2.3×10^{10} m^{-3} in the background, whereas the largest number concentration in the
483 street canyon is about 3.8×10^{10} m^{-3}.

484

5.2. Time-variant characteristics
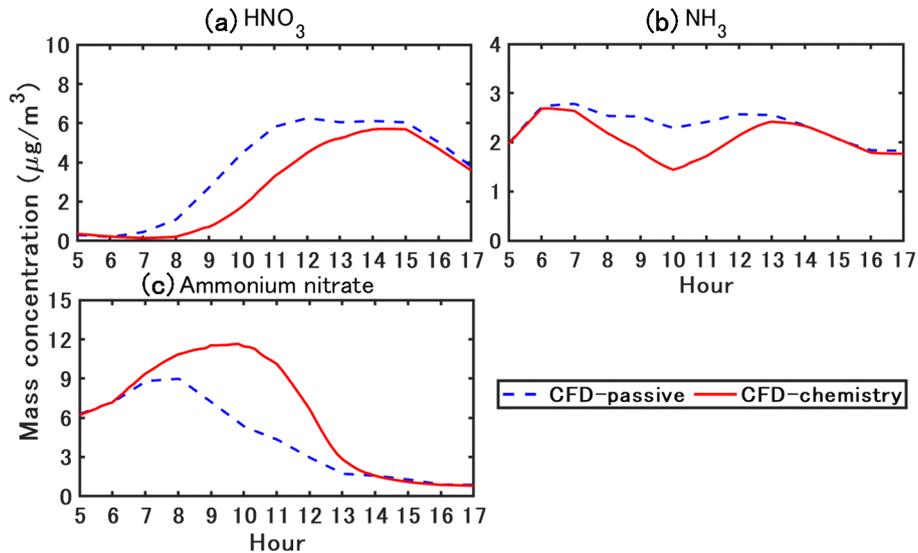
Fig. 14 Simulated time-varying concentrations of ammonium nitrate and precursor gas (HNO₃ and NH₃).

Fig. 14 shows the simulated time-varying concentrations of ammonium nitrate formed by the condensation of HNO_3 and NH_3. Based on the traffic fleet in the current study, NH_3 emission is approximately 1-2% of NOx emissions. Ammonium nitrate and HNO_3 are not emitted and differences between simulations with or without chemistry coupling are due to gas chemical reactions and phase change between the gas and particle. Phase change may be driven by NH_3 emissions, as well as the non-thermodynamic equilibrium of the background concentrations.

In CFD-passive, NH_3 concentration peaks around 7 a.m. as NOx because it is emitted by traffic. The peak in HNO_3 concentration is later in the morning, around 11 am. HNO_3 is formed from the oxidation of NO_2, which is emitted by traffic and is rapidly formed from NO traffic emissions. The formation of HNO_3 is slower than the formation of NO_2, and probably occurs at the regional scale, leading to a delay in the peak of HNO_3 concentration compared to NO_2 concentration. In CFD-chemistry, the temporal variations of HNO_3 concentration show large differences with CFD-passive because HNO_3 condenses with NH_3 to form ammonium nitrate during the daytime. As a result, the HNO_3 concentration peak in CFD-chemistry is later than that in CFD-passive (it is shifted from 11 a.m. to around 2 p.m.). The NH_3 concentration in CFD-passive peaks at 7 a.m. because of traffic emission and is stable from 7 a.m. to 1 p.m. and then decreases from 1 p.m. Meanwhile, the condensation in CFD-chemistry leads to lower concentration than in

509 CFD-passive during the daytime (between 7 a.m. and 1 p.m.).

510 For 12-hour time-averaged concentrations, ammonium nitrate increases by 46% in CFD-
511 chemistry compared with that in CFD-passive. Background ammonium nitrate
512 concentration (CFD-passive) peaks around the morning rush (7 to 8 a.m.) and then
513 decreases. Meanwhile, in CFD-chemistry, ammonium nitrate concentration peaks later
514 around 10 a.m., because of the large increase in HNO_3 between the traffic rush and 10
515 a.m. However, although HNO_3 concentration does not vary much between 11 a.m. and 3
516 p.m., the ammonium nitrate concentration decreases from 10 a.m. to a very small level
517 (lower than 1 $\mu g/m^3$) after 2 p.m. This decrease is probably linked to the temperature
518 increase during the daytime (Fig. 2(b)) and the relative humidity decrease, leading to a
519 decrease in the condensation rate (Stelson and Seinfeld, 1982).
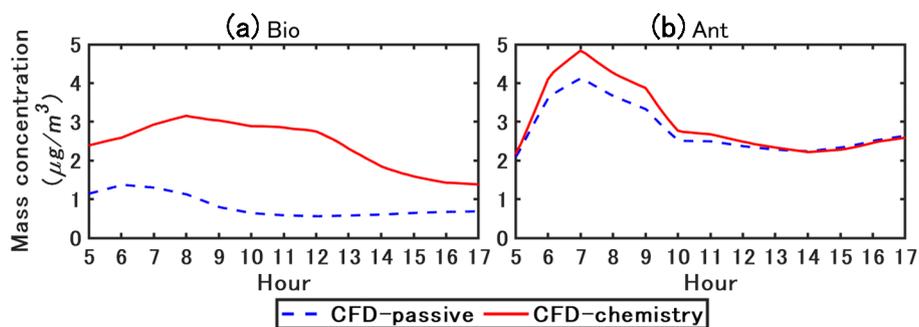
520
521 Fig. 15 Simulated time-varying concentration of organic matter. Bio refers to organic
522 matter formed from biogenic precursors. Ant refers to organic matter formed from
523 anthropogenic precursors.

524

525 Fig. 15 shows the simulated time-varying concentrations of organic matter. Organic
526 matter is divided into two main categories depending on the origin of the precursors: Bio
527 and Ant refer to the organic matter of biogenic and anthropogenic precursors respectively.
528 In CFD-chemistry, Bio concentration is larger than that in CFD-passive. As biogenic
529 precursors are not emitted in the street, the condensation of Bio is due to background
530 precursor gases. As discussed previously, the concentration of ammonium nitrate is higher
531 in CFD-chemistry than in CFD-passive, providing a larger aqueous mass onto which
532 hydrophilic compounds of the biogenic precursor gases condense. As the condensation of
533 ammonium nitrate decreases in the afternoon as shown in Fig. 14, the condensation of
534 Bio also decreases.

535 Ant is largely influenced by traffic emissions in the street, particularly by emissions of
536 semi-volatile compounds (Sartelet et al., 2018), which soon condenses after emissions.
537 Therefore there is a peak around 7 a.m. owing to the morning rush. In the model,
538 anthropogenic emissions are mostly hydrophobic, therefore the condensation is not

539   enhanced by the increase in inorganic concentrations. Consequently, the difference
540   between CFD-chemistry and CFD-passive is larger in the morning owing to the large
541   increase in traffic emissions, but small differences are observed in the afternoon.
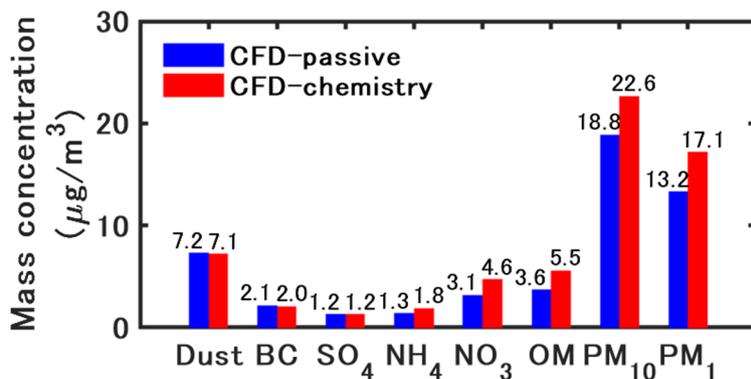
542
543   Fig. 16 Time-averaged concentration of PM_{10}, PM_1 and the chemical compounds of PM_{10}
544   from 5 a.m. to 5 p.m.
545
546   Fig. 16 shows the time-averaged concentrations of PM_{10}, PM_1 and the chemical
547   compounds of PM_{10} from 5 a.m. to 5 p.m. The time-averaged PM_{10} and PM_1
548   concentrations increase by approximately 3.8 $\mu g/m^3$ in CFD-chemistry compared to CFD-
549   passive, indicating that chemistry mainly influences small particles. Inert matter slightly
550   decreases in CFD-chemistry owing to dry deposition. Condensation increases of 48%,
551   38% and 53% of nitrate, ammonium and organic matter concentrations in CFD-chemistry
552   compared to CFD-passive.
553

554   *5.3. Size distribution of particle matter*
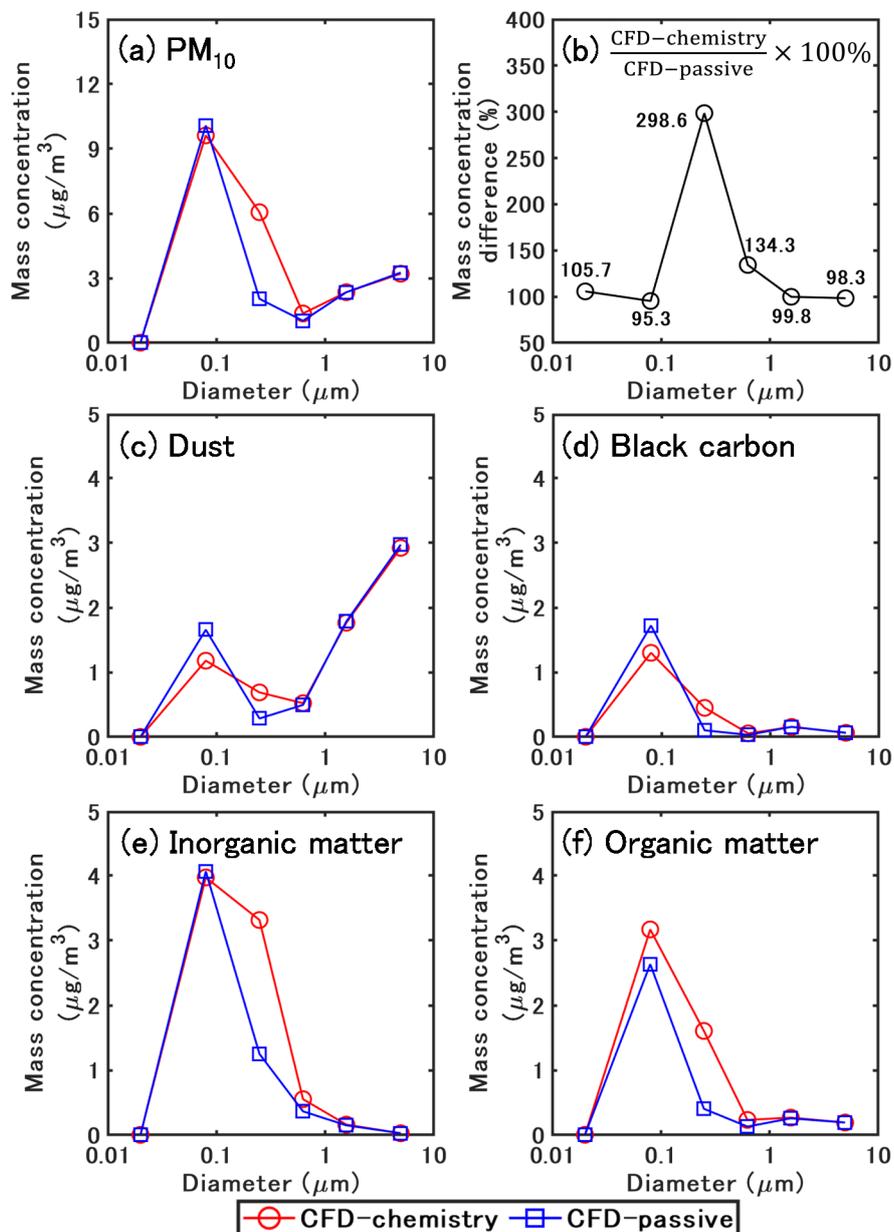
555
556   Fig. 17 Time-averaged size distribution of PM$_{10}$ for different chemical species from 5 a.m.
557   to 5 p.m.
558
559   Fig. 17 shows the time-averaged size distribution of PM$_{10}$ for the different chemical
560   compounds of particles from 5 a.m. to 5 p.m. The bound diameters are 0.01, 0.04, 0.16,
561   0.4, 1.0, 2.5 and 10 μm, and the mean diameters are 0.02, 0.08, 0.25, 0.63, 1.58 and 5.01
562   μm.
563   For the total concentration of PM$_{10}$ (Fig. 17(a)), the lowest and the largest concentrations
564   are in the first size section (0.01-0.04 μm) and the second size section (0.04-0.16 μm)

565   respectively, for both the CFD-passive and the CFD-chemistry simulations. Generally,
566   the loss and gain of mass concentration in each size section are related to emission, dry
567   deposition, coagulation (small particles coagulate into large particles), and
568   condensation/evaporation (phase exchange between gas and particles).

569   Fig. 17(b) shows the mass concentration ratio between CFD-passive and CFD-chemistry
570   for each size section. For particles in the size range of 0.04-0.16 μm, the concentrations
571   are smaller in CFD-chemistry than in CFD-passive, because dry deposition and
572   coagulation both decrease mass concentration for those particles. Furthermore, semi-
573   volatile gases may evaporate from small particles because of the Kelvin effect and
574   condense onto larger particles. For particles in the size range of 0.16-1.0 μm, the
575   concentrations are much larger in CFD-chemistry than CFD-passive, indicating that
576   coagulation and condensation on the mass-concentration increase are dominant to other
577   processes, such as deposition. For particles larger than 1 μm, the concentrations of CFD-
578   passive and CFD-chemistry are similar, because particle dynamics have a low influence
579   on large particles.

580   The size distribution of dust (Fig. 17(c)) shows that most dust mass concentrations are in
581   particles larger than 1 μm. Meanwhile, most of the mass concentration of BC, inorganic
582   and organic matter (Fig. 17(d-f)) is in particles smaller than 1 μm. Coagulation is the main
583   process influencing the size distribution for inert matter (dust and BC). Compared to
584   CFD-passive, the mass concentration of dust and BC in the second size section decrease
585   by 0.48 and 0.43 μg/m^3 in CFD-chemistry. Correspondingly, the mass concentrations of
586   dust and BC in the third size section increase by 0.41 and 0.35 μg/m^3.

587   For inorganic matter, in the second size section, the concentrations are similar in CFD-
588   passive and CFD-chemistry: particle dynamics decrease sulphate concentration by 0.32
589   μg/m^3 and increase nitrate concentration by 0.17 μg/m^3. However, as the results of the
590   combination effect of coagulation and ammonium nitrate condensation, the
591   concentrations largely increase in the third size section in CFD-chemistry: sulphate,
592   ammonium and nitrate increase by 0.27, 0.6 and 1.24 μg/m^3, respectively.

593   For organic matter, because of condensation of hydrophilic compounds from background
594   biogenic gases and anthropogenic emissions, CFD-chemistry leads to a small increase in
595   concentrations (0.53 μg/m^3) in the second size section and a large increase in the third
596   section (1.21 μg/m^3) compared to CFD-passive. In detail, Bio concentrations increase by
597   0.89 μg/m^3, and Ant concentrations decrease by 0.36 μg/m^3 in the second size section. In
598   the third size section, Bio and Ant concentrations increase by 0.67, 0.54 μg/m^3.

599

600 *5.4. Influence of ammonia traffic emissions*
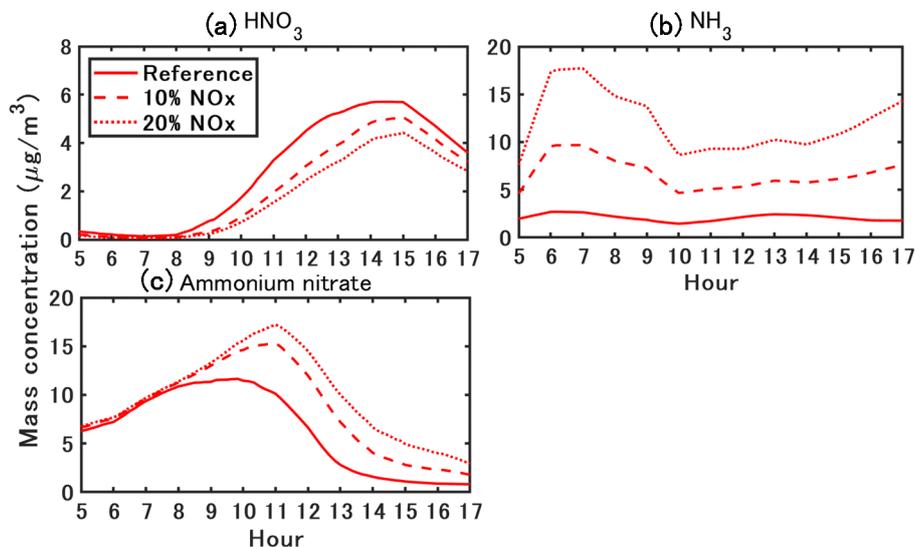
602 Fig. 18 Sensitivity of ammonium nitrate concentration to NH₃ emission.

603

604 Suarez-Bertoa et al. (2017) conducted on-road measurements of NH_3 emissions from two
605 Euro 6b compliant light duty cars (one gasoline and one diesel) under real-world driving
606 conditions, and they found that NH_3 emissions accounted for 11.9% and 0.92% of NOx
607 emissions for gasoline and diesel vehicles. As explained in Section 5.2, NH_3 emission
608 emissions are approximately 1-2% of NOx emissions in the reference case. Two cases are
609 considered to simulate the impact of an increase in the fraction of gasoline cars, and
610 sensitivity simulations are performed with NH_3 emission considered as 10% and 20% of
611 the NOx emissions.
612 Fig. 18 shows the sensitivity of ammonium nitrate concentration to NH_3 emissions. A
613 larger NH_3 emission delays the peak of ammonium nitrate by approximately one hour.
614 For a 12-hour average, considering NH_3 emissions of 10% and 20% of NOx emissions
615 leads to a large increase in ammonium nitrate (35% and 55%) compared to the reference
616 case, because of the formation of ammonium nitrate by the condensation of HNO_3 and
617 NH_3.
618

619 **6. Conclusions**
620 Particles in urban environment impose adverse impacts on pedestrians' health.
621 Conventional CFD methods regarding particles as passive scalars cannot reproduce the
622 formation of secondary aerosols and may lead to uncertain simulations. Therefore, to
623 increase the simulation accuracy of particle dispersion, we coupled the CFD software
624 OpenFOAM (OF) and Code_Saturne (CS) with SSH-Aerosol, a modular box model to

simulate the evolution of primary and secondary aerosols. The main processes involved in the aerosol dynamics (coagulation, condensation /evaporation and dry deposition) were considered.

We simulated a 12-hour transient dispersion of pollutants from traffic emissions in a street canyon using the unsteady RANS model. The simulation domain was generated to model a street-canyon where field measurements are available. The flow field was based on the WRF model. The background concentrations of gas and particles were obtained from regional-scale simulations with a chemistry-transport model. The particle diameter range (0.01 μm to 10 μm) was divided into six size sections. The following conclusions were drawn from the results of this study.

1) The simulated spatially-averaged values in the street canyon were validated from field measurement using validation metrics. For both OF and CS, the simulated NO_2 and PM_{10} concentrations based on the coupling model (CFD-chemistry) achieved better agreement with the measurement data than the conventional CFD simulation which considered pollutants as passive scalars (CFD-passive). The differences between of the OF and CS results were not obvious and were mainly due to the differences in the turbulence scheme. The following conclusions were drawn based on the simulated OF concentrations.

2) For the flow field, a large vortex was observed in the canyon with a small secondary vortex at the corner of the leeward wall at the current aspect ratio (H/W=0.31). In CFD-chemistry, because of the reverse flow, the 12-hour (from 5 a.m. to 5 p.m.) time-averaged NO_2 mass concentration, PM_{10} mass and number concentrations at pedestrian height were much higher near the leeward wall (116 μg/m^3, 28 μg/m^3, 3.2×10^{10} m^{-3}) than the background (26 μg/m^3, 15 μg/m^3, 2.3×10^{10} m^{-3}).

3) Secondary aerosol formation largely affected the mass concentration and size distribution of particle matter. For 12-hour time-averaged concentrations, ammonium nitrate and organic matter increased by 46% and 53% in CFD-chemistry compared to CFD-passive because of condensation of HNO_3 and NH_3, background biogenic precursor-gases and anthropogenic precursor-gas emissions. Coagulation largely influenced the size distribution of small particles by combining particles with a diameter of 0.04-0.16 μm into 0.16-0.4 μm. At the same time, CFD-chemistry showed a much larger concentration than CFD-passive for the particles in 0.16-1.0 μm, indicating that the effect of condensation on increasing mass concentration was dominant compared to other chemical processes.

4) Urban areas are NH_3-limited (HNO_3 sufficient) areas, therefore, increasing NH_3 leads to a large increase in ammonium nitrate. Vehicles are considered to be the main

661   source of NH_3 in urban environments. Increasing the fleet's proportion of recent
662   gasoline vehicles may increase NH_3 emissions. For a 12-hour average, we considered
663   NH_3 emissions of 10% and 20% of NOx emissions led to a large increase in
664   ammonium nitrate (35% and 55%) compared to the reference case which considers
665   NH_3 emission as 1-2% of NOx emissions.
666 5) A grid sensitivity analysis showed that the particles' concentrations of inorganic and
667   organic compounds were sensitive to grid resolution, whereas inert particle
668   concentrations were not sensitive to grid resolution. In addition, simulated values
669   based on a grid size of 0.5 m in the street canyon showed small differences with a
670   grid size of 0.25 m, indicating that a spatial resolution of 0.5 m can be enough for
671   reactive particle dispersion at the street level.
672 6) Operator splitting is often employed to solve the transport term and chemical
673   reactions over a given time step in chemical transport simulations. Two integration
674   orders were considered: A-B splitting method (CFD(Δt)-Chemistry(Δt)) and A-B-A
675   splitting method (CFD($\Delta t/2$)-Chemistry(Δt)-CFD($\Delta t/2$)). The results showed that
676   the A-B-A splitting method had almost the same concentrations as the A-B splitting
677   method with half the computational time. Further sensitivity analysis on the time step
678   showed that a time step of 0.5 s was enough when using the A-B-A splitting method.
679 7) Conducting a CFD simulation with constant boundary conditions and emission rates
680   at a specific time point is considered a practical method to achieve time-averaged
681   concentrations for evaluating street-level pollutant concentrations. The validation
682   was conducted using conditions on five time points (7 a.m., 10 a.m., 1 p.m., 3 p.m.
683   and 5 p.m.). The simulated concentration based on the above method exhibited
684   almost the same value as the simulation with transient conditions at the same time
685   points.
686 The limitation of this study should be addressed as several reasonable approximations
687 and assumptions were made in the simulation settings.
688 1) Concerning the simulation domain: since we focused on the coupling of gas chemical
689   reactions and particle dynamics to the CFD codes, we selected a 12-hour period when
690   wind direction was perpendicular to the street. In that case, a 2-D simplification of
691   the simulation domain is reasonable, as shown by Maison et al. (2022). However, in
692   more general cases, the pollutant residence time for a 3-D canyon could be shorter
693   compared to the 2-D canyon adopted in this study, and the effects of chemical
694   reaction or aerosol processes could be weaker than this study reported. In addition,
695   various wind directions should be considered to better evaluate the performance of
696   the coupled model. Further work will focus on the application of the coupled model

697   to a complex urban environment with changing wind directions.

698   2) Concerning the physical model: the simulations were based on RANS-closure, and

699   the SSH-aerosol processed the ensemble-averaged concentration, therefore the

700   covariance of turbulent diffusion and chemical reaction may not be fully reproduced.

701   The simulation based on LES may provide better prediction of second-order

702   quantities. In addition, the radiation on the wall may lead street-level-variations of

703   temperature and could affect the flow field and chemical reaction rates. However,

704   this was not considered here, and the radiation effect on the local temperature was

705   simplified as being the same as in the inflow condition. The inflow temperature was

706   obtained from WRF model where the radiation was considered, and the time variation

707   of temperature was considered to be the same as the background.

708   Future work will be conducted on the influence of environmental factors and emission

709   conditions, aiming to provide knowledge to devise suitable countermeasures to decrease

710   particle concentration in microscale urban environments.

711

712   Acknowledgments: This work benefited from discussions with Bertrand Carissimo. The

713   authors acknowledge funding from DIM QI^2 (Air Quality Research Network on air

714   quality in the Île-de-France region) and from Île-de-France region.

715

716   Code/Data availability

717   The codes used in this publication are available to the community, and they can be

718   accessed by request to the corresponding author.

719

720   Author contribution

721   KS and RO were responsible for conceptualization. CL, YW, CF, KS, YK and ZW

722   developed the software. CL and YW conduced the visualization and validation; CL, YW

723   and KS performed the formal analysis. KS and RO acquired resources. CL, YW, RO and

724   KS were responsible for writing and original draft preparation. CF, YK, HK reviewed and

725   edited the manuscript All co-authors contributed to the discussion of the paper.

726

727   Competing interests

728   The contact author has declared that neither they nor their co-authors have any

729   competing interests.

730

731   Reference

732   Anenberg, S. C., Miller, J., Minjares, R., Du, L., Henze, D. K., Lacey, F., Malley, C. S.,

733   Emberson, L., Franco, V., Klimont, Z., and Heyes, C.: Impacts and mitigation of excess

734   diesel-related NO x emissions in 11 major vehicle markets, Nature, 545, 467–471,

735   https://doi.org/10.1038/nature22086, 2017.

736   EMEP/EEA: EMEP/EEA air pollutant emission inventory guidebook 2019, EEA Report

737   No 13/2019, European Environment Agency:

738   https://www.eea.europa.eu/publications/emep-eea-guidebook-2019, last access: 14

739   March 2022.

740   Archambeau, F., Méchitoua, N., and Sakiz, M.: Code Saturne: A Finite Volume Code for

741   Turbulent flows - Industrial Applications, International Journal on Finite Volumes, 1,

742   2004.

743   Arpaci, V. S. and Larsen, P. S.: Convection Heat Transfer, Prentice Hall, New York,

744   1984.

745   Belcher, S. E.: Mixing and transport in urban areas, Philosophical Transactions of the

746   Royal Society A: Mathematical, Physical and Engineering Sciences, 363, 2947–2968,

747   https://doi.org/10.1098/rsta.2005.1673, 2005.

748   Bishop, G. A. and Stedman, D. H.: Reactive Nitrogen Species Emission Trends in Three

749   Light-/Medium-Duty United States Fleets, Environ Sci Technol, 49, 11234–11240,

750   https://doi.org/10.1021/acs.est.5b02392, 2015.

751   Blackman, K., Perret, L., and Savory, E.: Effect of upstream flow regime on street

752   canyon flow mean turbulence statistics, Environmental Fluid Mechanics, 15, 823–849,

753   https://doi.org/10.1007/s10652-014-9386-8, 2015.

754   Blocken, B., Tominaga, Y., and Stathopoulos, T.: CFD simulation of micro-scale

755   pollutant dispersion in the built environment, Build Environ, 64, 225–230,

756   https://doi.org/10.1016/j.buildenv.2013.01.001, 2013.

757   Boutahar, J., Lacour, S., Mallet, V., Quelo, D., Roustan, Y., and Sportisse, B.:

758   Development and validation of a fully modular platform for numerical modelling of air

759   pollution: POLAIR, Int J Environ Pollut, 22, 17,

760   https://doi.org/10.1504/IJEP.2004.005474, 2004.

761   Chang, J. C. and Hanna, S. R.: Air quality model performance evaluation, Meteorology

762   and Atmospheric Physics, 87, 167–196, https://doi.org/10.1007/s00703-003-0070-7,

763   2004.

764   Du, Y., Xu, X., Chu, M., Guo, Y., and Wang, J.: Air particulate matter and

765   cardiovascular disease: The epidemiological, biomedical and clinical evidence,

766   https://doi.org/10.3978/j.issn.2072-1439.2015.11.37, 2016.

767   Ferrero, E., Alessandrini, S., Anderson, B., Tomasi, E., Jimenez, P., and Meech, S.:

768   Lagrangian simulation of smoke plume from fire and validation using ground-based

769   lidar and aircraft measurements, Atmos Environ, 213, 659–674,

770   https://doi.org/10.1016/j.atmosenv.2019.06.049, 2019.

771   Fu, K. and Liang, D.: The conservative characteristic FD methods for atmospheric

772   aerosol transport problems, J Comput Phys, 305, 494–520,

773   https://doi.org/10.1016/j.jcp.2015.10.049, 2016.

774   Gao, S., Kurppa, M., Chan, C. K., and Ngan, K.: Technical note: Dispersion of cooking-

775   generated aerosols from an urban street canyon, Atmos Chem Phys, 22, 2703–2726,

776   https://doi.org/10.5194/acp-22-2703-2022, 2022.

777   Guimet, V. and Laurence, D.: A linearised turbulent production in the k-ε model for

778   engineering applications, in: Engineering Turbulence Modelling and Experiments 5,

779   edited by: Rodi, W. and Fueyo, N., Elsevier Science Ltd, Oxford, UK, 157–166, 2002.

780   Hanna, S. R., Hansen, O. R., and Dharmavaram, S.: FLACS CFD air quality model

781   performance evaluation with Kit Fox, MUST, Prairie Grass, and EMU observations,

782   Atmos Environ, 38, 4675–4687, https://doi.org/10.1016/j.atmosenv.2004.05.041, 2004.

783   Harten, A.: On a Class of High Resolution Total-Variation-Stable Finite-Difference

784   Schemes, SIAM J Numer Anal, 21, 1–23, https://doi.org/10.1137/0721001, 1984.

785   Jones, A. M., Yin, J., and Harrison, R. M.: The weekday–weekend difference and the

786   estimation of the non-vehicle contributions to the urban increment of airborne

787   particulate matter, Atmos Environ, 42, 4467–4479,

788   https://doi.org/10.1016/j.atmosenv.2008.02.001, 2008.

789   Kim, M. J.: Sensitivity of nitrate aerosol production to vehicular emissions in an urban

790   street, Atmosphere (Basel), 10, 212, https://doi.org/10.3390/ATMOS10040212, 2019.

791   Kim, M. J., Park, R. J., Kim, J. J., Park, S. H., Chang, L. S., Lee, D. G., and Choi, J. Y.:

792   Computational fluid dynamics simulation of reactive fine particulate matter in a street

793   canyon, Atmos Environ, 209, 54–66, https://doi.org/10.1016/j.atmosenv.2019.04.013,

794   2019.

795   Kim, Y., Wu, Y., Seigneur, C., and Roustan, Y.: Multi-scale modeling of urban air

796   pollution: development and application of a Street-in-Grid model (v1.0) by coupling

797   MUNICH (v1.0) and Polair3D (v1.8.1), Geosci Model Dev, 11, 611–629,

798   https://doi.org/10.5194/gmd-11-611-2018, 2018.

799   Kim, Y., Lugon, L., Maison, A., Sarica, T., Roustan, Y., Valari, M., Zhang, Y., André,

800   M., Sartelet, K., Paris-saclay, U., and Ecosys, U. M. R.: MUNICH v2.0: A street-

801   network model coupled with SSH-aerosol (v1.2) for multi-pollutant modelling, Geosci

802   Model Dev, 2022.

803   Kumar, P., Fennell, P., Langley, D., and Britter, R.: Pseudo-simultaneous measurements

804   for the vertical variation of coarse, fine and ultrafine particles in an urban street canyon,

Atmos Environ, 42, 4304–4319, https://doi.org/10.1016/j.atmosenv.2008.01.010, 2008.

Kurppa, M., Hellsten, A., Roldin, P., Kokkola, H., Tonttila, J., Auvinen, M., Kent, C., Kumar, P., Maronga, B., and Järvi, L.: Implementation of the sectional aerosol module SALSA2.0 into the PALM model system 6.0: Model development and first evaluation, Geosci Model Dev, 12, 1403–1422, https://doi.org/10.5194/gmd-12-1403-2019, 2019.

Lo, K. W. and Ngan, K.: Characterising the pollutant ventilation characteristics of street canyons using the tracer age and age spectrum, Atmos Environ, 122, 611–621, https://doi.org/10.1016/j.atmosenv.2015.10.023, 2015.

Lo, K. W. and Ngan, K.: Characterizing ventilation and exposure in street canyons using Lagrangian particles, J Appl Meteorol Climatol, 56, 1177–1194, https://doi.org/10.1175/JAMC-D-16-0168.1, 2017.

Lugon, L., Vigneron, J., Debert, C., Chrétien, O., and Sartelet, K.: Black carbon modeling in urban areas: investigating the influence of resuspension and non-exhaust emissions in streets using the Street-in-Grid model for inert particles (SinG-inert), Geosci Model Dev, 14, 7001–7019, https://doi.org/10.5194/gmd-14-7001-2021, 2021a.

Lugon, L., Sartelet, K., Kim, Y., Vigneron, J., and Chretien, O.: Simulation of primary and secondary particles in the streets of Paris using MUNICH, Faraday Discuss, 226, 432–456, https://doi.org/10.1039/d0fd00092b, 2021b.

Maison, A., Flageul, C., Carissimo, B., Wang, Y., Tuzet, A., and Sartelet, K.: Parameterizing the aerodynamic effect of trees in street canyons for the street network model MUNICH using the CFD model Code_Saturne, Atmos Chem Phys, 22, 9369–9388, https://doi.org/10.5194/acp-22-9369-2022, 2022.

OpenFOAM user guide: https://www.openfoam.com/.

Parente, A., Gorlé, C., van Beeck, J., and Benocci, C.: Improved k–ε model and wall function formulation for the RANS simulation of ABL flows, Journal of Wind Engineering and Industrial Aerodynamics, 99, 267–278, https://doi.org/10.1016/j.jweia.2010.12.017, 2011.

Di Sabatino, S., Buccolieri, R., Pulvirenti, B., and Britter, R.: Simulations of pollutant dispersion within idealised urban-type geometries with CFD and integral models, Atmos Environ, 41, 8316–8329, https://doi.org/10.1016/j.atmosenv.2007.06.052, 2007.

Sartelet, K., Zhu, S., Moukhtar, S., André, M., André, J. M., Gros, V., Favez, O., Brasseur, A., and Redaelli, M.: Emission of intermediate, semi and low volatile organic compounds from traffic and their impact on secondary organic aerosol concentrations over Greater Paris, Atmos Environ, 180, 126–137, https://doi.org/10.1016/j.atmosenv.2018.02.031, 2018.

Sartelet, K., Couvidat, F., Wang, Z., Flageul, C., and Kim, Y.: SSH-aerosol v1.1: A

841 modular box model to simulate the evolution of primary and secondary aerosols,

842 Atmosphere (Basel), 11, 525, https://doi.org/10.3390/atmos11050525, 2020.

843 Sartelet, K. N., Debry, E., Fahey, K., Roustan, Y., Tombette, M., and Sportisse, B.:

844 Simulation of aerosols and gas-phase species over Europe with the Polyphemus system:

845 Part I-Model-to-data comparison for 2001, Atmos Environ, 41, 6116–6131,

846 https://doi.org/10.1016/j.atmosenv.2007.04.024, 2007.

847 Sportisse, B.: An Analysis of Operator Splitting Techniques in the Stiff Case, J Comput

848 Phys, 161, 140–168, https://doi.org/10.1006/jcph.2000.6495, 2000.

849 Stelson, A. W. and Seinfeld, J. H.: Relative humidity and temperature dependence of the

850 ammonium nitrate dissociation constant, Atmospheric Environment (1967), 16, 983–

851 992, https://doi.org/10.1016/0004-6981(82)90184-6, 1982.

852 Suarez-Bertoa, R. and Astorga, C.: Impact of cold temperature on Euro 6 passenger car

853 emissions, Environmental Pollution, 234, 318–329,

854 https://doi.org/10.1016/j.envpol.2017.10.096, 2018.

855 Suarez-Bertoa, R., Mendoza-Villafuerte, P., Riccobono, F., Vojtisek, M., Pechout, M.,

856 Perujo, A., and Astorga, C.: On-road measurement of NH 3 emissions from gasoline and

857 diesel passenger cars during real world driving conditions, Atmos Environ, 166, 488–

858 497, https://doi.org/10.1016/j.atmosenv.2017.07.056, 2017.

859 Sun, K., Tao, L., Miller, D. J., Pan, D., Golston, L. M., Zondlo, M. A., Griffin, R. J.,

860 Wallace, H. W., Leong, Y. J., Yang, M. M., Zhang, Y., Mauzerall, D. L., and Zhu, T.:

861 Vehicle Emissions as an Important Urban Ammonia Source in the United States and

862 China, Environ Sci Technol, 51, 2472–2481, https://doi.org/10.1021/acs.est.6b02805,

863 2017.

864 Sung, J. C., Pulliam, B. L., and Edwards, D. A.: Nanoparticles for drug delivery to the

865 lungs, Trends Biotechnol, 25, 563–570, https://doi.org/10.1016/j.tibtech.2007.09.005,

866 2007.

867 Tominaga, Y. and Stathopoulos, T.: Turbulent Schmidt numbers for CFD analysis with

868 various types of flowfield, Atmos Environ, 41, 8091–8099,

869 https://doi.org/10.1016/j.atmosenv.2007.06.054, 2007.

870 Tominaga, Y. and Stathopoulos, T.: CFD simulation of near-field pollutant dispersion in

871 the urban environment: A review of current modeling techniques, Atmos Environ, 79,

872 716–730, https://doi.org/10.1016/j.atmosenv.2013.07.028, 2013.

873 Trini Castelli, S., Armand, P., Tinarelli, G., Duchenne, C., and Nibart, M.: Validation of

874 a Lagrangian particle dispersion model with wind tunnel and field experiments in urban

875 environment, Atmos Environ, 193, 273–289,

876 https://doi.org/10.1016/j.atmosenv.2018.08.045, 2018.

877 Wesely, M. L.: Parameterization of surface resistances to gaseous dry deposition in

878 regional-scale numerical models, Atmospheric Environment (1967), 23, 1293–1304,

879 https://doi.org/10.1016/0004-6981(89)90153-4, 1989.

880 Wu, L., Hang, J., Wang, X., Shao, M., and Gong, C.: APFoam 1.0: Integrated

881 computational fluid dynamics simulation of O3-NOx-volatile organic compound

882 chemistry and pollutant dispersion in a typical street canyon, Geosci Model Dev, 14,

883 4655–4681, https://doi.org/10.5194/gmd-14-4655-2021, 2021.

884 Yakhot, V., Orszag, S. A., Thangam, S., Gatski, T. B., and Speziale, C. G.: Development

885 of turbulence models for shear flows by a double expansion technique, Physics of Fluids

886 A, 4, 1510–1520, https://doi.org/10.1063/1.858424, 1992.

887 Yee, H. C.: Construction of explicit and implicit symmetric TVD schemes and their

888 applications, J Comput Phys, 68, 151–179, https://doi.org/10.1016/0021-

889 9991(87)90049-0, 1987.

890 Zhang, K., Chen, G., Zhang, Y., Liu, S., Wang, X., Wang, B., and Hang, J.: Integrated

891 impacts of turbulent mixing and NOX-O3 photochemistry on reactive pollutant

892 dispersion and intake fraction in shallow and deep street canyons, Science of The Total

893 Environment, 712, 135553, https://doi.org/10.1016/j.scitotenv.2019.135553, 2020.

894 Zhang, L., Gong, S., Padro, J., and Barrie, L.: A size-segregated particle dry deposition

895 scheme for an atmospheric aerosol module, Atmos Environ, 35, 549–560,

896 https://doi.org/10.1016/S1352-2310(00)00326-5, 2001.

897 Zhang, L., Brook, J. R., and Vet, R.: A revised parameterization for gaseous dry

898 deposition in air-quality models, Atmos Chem Phys, 3, 2067–2082,

899 https://doi.org/10.5194/acp-3-2067-2003, 2003.

900

901 Appendix A

902 The schemes for particle deposition velocity v_d were added to the transport equations

903 using volume sink terms based on (Zhang et al., 2001) and can be represented as:

$$v_{d,p} = \begin{cases} v_g + \dfrac{1}{R_a + R_s}, & \text{Wall surfaces} \\ v_g, & \text{Entire field} \end{cases} \tag{A1}$$

$$v_g = \frac{\rho d_p^2 g C}{18\eta} \tag{A2}$$

$$R_a = \frac{\ln(z_R/z_0) - \psi_H}{\kappa u_*} \tag{A3}$$

$$R_s = \frac{1}{\varepsilon_0 u_*(E_B + E_{IM} + E_{IN})R_1} \tag{A4}$$

904   The deposition velocity for the particles $v_{d,p}$ consists of both gravitational settling and
905   surface deposition near the wall surfaces. The gravitational settling velocity v_g was
906   considered for the entire field, ρ is the particle density; d_p is the particle diameter; g
907   is the acceleration of gravity; C is Cunningham correction factor for small particles; η
908   is the viscosity coefficient of air.
909   The aerodynamic resistance R_a is calculated from the first-layer-height z_R, roughness
910   length z_0, Von Kármán constant κ, friction velocity u_* and stability function ψ_H. For the
911   k–ε model, u_* is estimated by $\left(C_\mu^{0.5}k\right)^{0.5}$ and $C_\mu = 0.09$ is a constant of the model.
912   The surface resistance R_s is calculated from u_*, the collection efficiency from Brownian
913   diffusion E_B, the impaction E_{IM} and the interception E_{IN}. The correction factor
914   represents the fraction of particles that stick to the surface R_1 and an empirical
915   constant $\varepsilon_0 = 3$.
916   The dry deposition schemes for gas were added to the transport equations using volume
917   sink terms based on (Wesely, 1989) and (Zhang et al., 2003),which can be represented as:

$$v_{d,g} = \frac{1}{R_a + R_b + R_c} \tag{A5}$$

$$R_b = \frac{2}{\kappa u_*}\left(\frac{Sc}{Pr}\right)^{2/3} \tag{A6}$$

918   The deposition velocity for gas $v_{d,g}$ is calculated from the aerodynamic resistance R_a,
919   the quasi-laminar layer resistance R_b and the surface resistance for gas R_c. $Sc = v/D$
920   and $Pr = 0.72$ are the Schmidt and Prandtl number. v is the kinematic viscosity of air
921   and D is the molecular diffusivity of different gases. R_c is calculated based on (Zhang
922   et al., 2003).
923

924 Appendix B
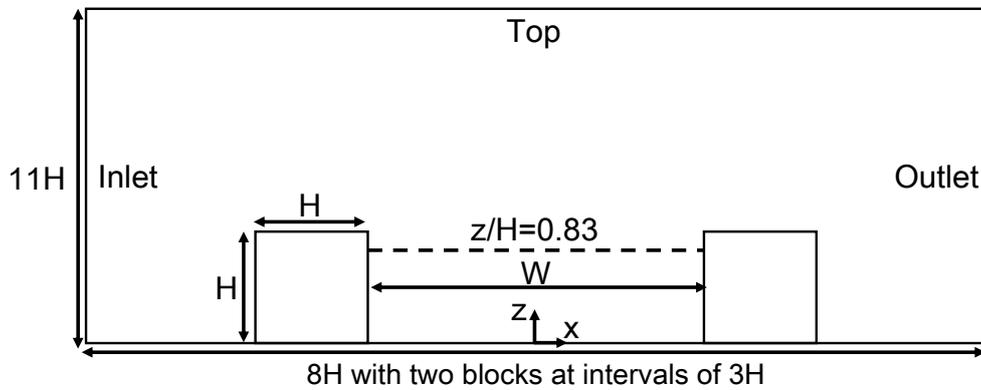
925

926 Fig. S1 Simulation domain for velocity validation.

927

928 Correctly representing the flow field in the street canyon is important to model accurately
929 the concentrations. Unfortunately, observation data on wind velocity is the street is not
930 available. Therefore, we conducted a velocity validation for OpenFOAM v2012 using
931 data from a wind tunnel experiment (Blackman et al., 2015). The 2-D simulation domain
932 is shown in Fig. S1. The aspect ratio in the experiment (H/W=0.33) is close to this study
933 (H/W=0.31). The building height H is 0.06 m. The grid size is 1/20 H in x- and z-
934 directions in the simulation domain under $3H$. The free-stream velocity U_{ref} is 5.9 m/s.
935 The steady-state flow field is simulated with the same turbulence model (RNG k–ε model)
936 as in the paper, and cyclic boundary conditions are used for the inlet and outlet. The slip
937 boundary is considered for the top, and non-slip boundary conditions with the same wall
938 functions as in the paper are considered for other walls.
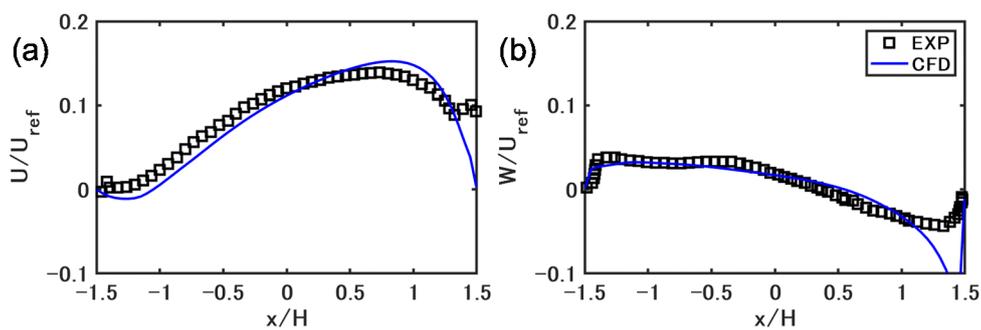
939

940 Fig. S2 Streamwise and vertical direction of mean wind velocities at $z/H = 0.83$.

941

942 Fig. S2 compares the simulated streamwise and vertical direction of mean wind velocities
943 with the experimental values at $z/H = 0.83$. The RNG k–ε model reproduce well the
944 velocities, although the velocities very close to the windward wall show differences with

945   the experimental values. The above validation shows that if suitable inlet conditions are
946   given, the flow field is well reproduced with the turbulence model adopted in this study.